Advanced Composites and Hybrid Materials (2022) 5:2378–2386
https://doi.org/10.1007/s42114-022-00443-0

ORIGINAL RESEARCH

Fluorescent probe of nitrogen-doped carbon dots derived from biomass for the sensing of MnO_4^- in polluted water based on inner filter effect

Wenjing Chen[1] · Hong Lin[1] · Yunying Wu[1] · Meng Yang[1] · Xianjing Zhang[1] · Shihua Zhu[1] · Maoting He[1] · Jianxin Xie[1] · Zhengjun Shi[2]

Received: 28 December 2021 / Revised: 22 February 2022 / Accepted: 27 February 2022 / Published online: 15 March 2022

Abstract

Nitrogen-doped carbon dots (N-CDs) were prepared from A*uricularia auricula* (L.ex Hook.) Underw via a one-step hydrothermal method. The N-CDs were spherical with an average particle size of 2.85 nm. The optimal excitation and emission wavelengths were 324 nm and 400 nm, respectively. There was considerable overlap between the excitation or emission spectrum of N-CDs and the UV absorption band of MnO_4^-. The inner filter effect (IFE) was formed between N-CDs and MnO_4^-, which led to the fluorescence quenching of N-CDs. The fluorescence quenching intensity of the system showed a good linear relationship with the concentration of MnO_4^- from 0.15 to 9.00 μM, and the limit of detection (LOD) of MnO_4^- was 0.12 μM. The proposed method was then used to measure MnO_4^- in polluted water with recoveries of 99.42 to 101.16%. The synthesized N-CDs offering trace MnO_4^- detection in simulation sample are extremely profound for environmental evaluation.

Keywords Nitrogen-doped carbon dots · A*uricularia auricula* (L.ex Hook.) Underw · MnO_4^- · Fluorescence quenching · Inner filter effect

1 Introduction

Potassium permanganate ($KMnO_4$) is a strong oxidant and is usually used as a disinfectant and antiseptic; it is widely applied in daily life and industry, e.g., treating polluted water and diseases in fish [1, 2]. MnO_4^- also is toxic, corrosive, and carcinogenic [3], and excess MnO_4^- can lead to skin irritation, neurological disorder, respiratory damage, gastrointestinal distress, and even genetic mutation [3, 4], and thus excess MnO_4^- can be seriously harmful to human health [5]. Accordingly, selective and sensitive determination of MnO_4^- in polluted water is critical for environmental evaluation [6]. A variety of detection methods have been developed such as flame atomic absorption spectrophotometry [7, 8], inductively coupled plasma-mass spectrometry [9, 10], and electrochemistry [11]. However, most of these techniques require sophisticated equipment and a skilled operator and are time-consuming. By contrast, fluorescent methods merited with simple operations and a fast response. Hence, novel fluorescent sensors to detect trace MnO_4^- in simulation samples are urgently needed. Currently, the MnO_4^- determination can be done by precious metal nanoclusters [12], organic layer [13], metal organic framework [14, 15], coordination polymer [16, 17], etc. However, the above fluorescent probes are usually toxic and harmful, complicated in synthesis process or expensive. To overcome the above limitations, it is necessary to seek a convenient, low toxicity, economic fluorescent material with high fluorescence quantum yield.

Carbon dots (CDs) have attracted widespread attention due to their low cytotoxicity, high biocompatibility, good chemical and photo-stability, easy preparation methods, and tunable emission [18–20]. They have been widely used in drug delivery [21], sensing [22–24], bioimaging [25], photocatalysis [26], electromagnetic composites [27–32],

✉ Jianxin Xie
xjx11228@163.com

✉ Zhengjun Shi
shizhengjun1979@163.com

[1] College of Chemistry Biology and Environment, Yuxi Normal University, Yuxi 653100, China

[2] Key Laboratory for Forest Resources Conservation and Utilization in the Southwest Mountains of China, Ministry of Education, Southwest Forestry University, Kunming 650224, China

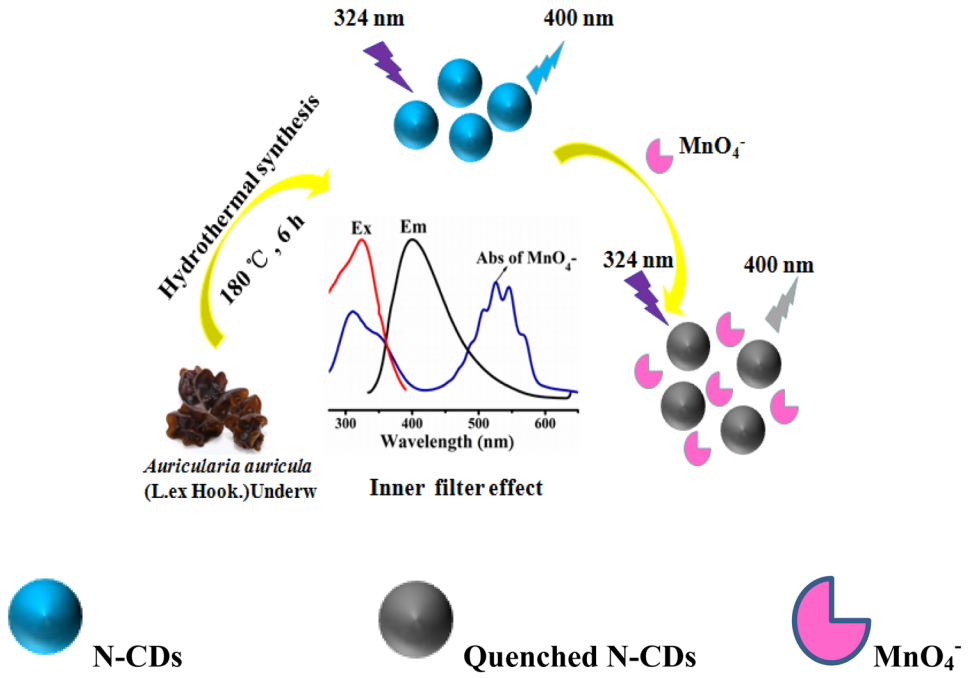

Scheme 1 Preparation method for the N-CDs and the detection of MnO_4^- based on the IFE

and optoelectronic devices [33–36]. Nitrogen doping is one of the most widely used strategies to improve the optical properties of CDs. Precursor materials for the preparation of nitrogen-doped CDs (N-CDs) include biomass and synthetic chemicals. Biomass stands out due to its low cytotoxicity, favorable biocompatibility, renewability, cost-effectiveness, and environment-friendly nature (relative to synthetic chemicals) [37–41]. Biomass is rich in proteins and carbohydrates, which are sources of nitrogen and carbon for N-CD preparation. Accordingly, N-CDs can be easily prepared from biomass without the addition of nitrogen and passivators. Numerous N-CDs have been reported which were prepared using natural biomass as precursor, including oyster mushroom [42], palm powder [43], leek [44], rice husk [45], and Aegle Marmelos [46].

In this work, a facile one-step hydrothermal method was reported for the synthesis of N-CDs using A*uricularia auricula* (L.ex Hook.) Underw as the sole precursor. The N-CDs were successfully used in the determination of MnO_4^- in polluted water based on the inner filter effect (IFE), as displayed in Scheme 1.

2 Experimental

2.1 Materials

The *Auricularia auricula* (L.ex Hook.) Underw used here was purchased from a local supermarket. Quinine sulfate was purchased from Aladdin. Other analytical-grade chemicals were from Xilong Chemical Co. Ltd. without further purification. Ultrapure water was used throughout. Polluted water was collected from Bosi lake on our campus. Before use, the polluted water was centrifuged at 5000 rpm for 10 min, and then filtered through a 0.2-μm filtration membrane.

2.2 Instrument

Transmission electron microscopy (FEI f 20, USA) was used to obtain the morphological features of the N-CDs. A Bruker D8 Advance X-ray diffractometer (Bruker, Germany) was used to evaluate the crystalline structure. A PerkinElmer Fourier transform infrared spectrometer (PerkinElmer, USA) was used to analyze the surface functional groups. XPS spectra were acquired on an EscaLab 250Xi X-ray photoelectron spectroscopy system (Thermo Fisher Scientific, USA). UV–vis absorption spectra and fluorescence spectra were obtained using a Shimadzu 2550 UV–vis spectrometer (Shimadzu, China) and a Hitachi FL-7000 fluorescence spectrophotometer (Hitachi, Japan), respectively. Fluorescence lifetime measurements were obtained with a Horiba FluoroMax-4 fluorescence spectrophotometer (Horiba, Japan). The analysis of the above data was conducted on origin 9.0.

2.3 Synthesis of N-CDs

Here, 1.0000 g of crushed *Auricularia auricula* (L.ex Hook.) Underw powder and 20 mL of ultrapure water were transferred into a 100-mL Teflon-lined autoclave and heated at 180 °C for 6 h. After the Teflon-lined autoclave was cooled to room temperature, the brown N-CD solution was first filtered

with filter paper and then centrifuged at 5000 rpm for 10 min. The material was then filtered through a 0.2-μm filtration membrane and finally dialyzed with a 500-Da dialysis membrane for 24 h. The pure N-CD solution was dried in a vacuum oven, and a brown solid was obtained. The N-CDs were then dissolved in ultrapure water and stored at 4 °C for later use.

2.4 MnO_4^- detection based on N-CDs

MnO_4^- stock solution (3 mM) was prepared and quantitatively diluted with ultrapure water. Next, 200 μL of pure N-CD solution and different amounts of MnO_4^- solution were transferred into a 1-cm quartz cuvette, and the mixture was diluted with PBS buffer solution (pH = 2) to a final volume of 2 mL, this was then mixed thoroughly. The mixed solution was then incubated for 20 min at room temperature. The fluorescence spectra of the above solutions were recorded from 334 to 550 nm under 324 nm excitation. Each experiment was measured three times.

3 Results and discussion

3.1 Characterization of the N-CDs

N-CDs were synthesized from *Auricularia auricula* (L.ex Hook.) Underw via a one-step hydrothermal method. A high-resolution transmission electron microscope (HR-TEM) was used to characterize the morphology of the N-CDs. Figure 1a and b show that the N-CDs were spherical with good dispersion in aqueous solution and had a uniform particle size. The average particle size of the N-CDs is about 2.85 nm. There was a diffuse peak centered at 23.5 (2θ value) in the XRD pattern of the N-CDs (Fig. S1), suggesting the amorphous nature of the synthesized N-CDs [47].

The surface functional groups of the N-CDs were identified by XPS and FT-IR. In the FT-IR spectrum of the N-CDs (Fig. 1c), the peaks at 3399 cm^{-1} and 2933 cm^{-1} were assigned to the stretching vibrations of O–H/N–H, and C-H. The peaks at 1731–1613 cm^{-1} and 1415–1376 cm^{-1} were related to C = O and C-N, respectively. Peaks at 1248 cm^{-1} and 1036 cm^{-1} were contributed to the characteristic absorption band of C-O. The surface chemical groups and elemental analysis of N-CDs were further identified by XPS. Figure 1d shows three peaks located at 284.8 eV, 399.8 eV, and 531.7 eV, which illustrated that the N-CDs mainly included C (64.69%), N (9.48%), and O (25.83%). The C1s spectrum of N-CDs (Fig. S2) revealed three peaks at 284.8 eV, 286.2 eV, and 287.8 eV due to C–C/C = C, C-O, and C = O, respectively. The N1s spectrum of N-CDs (Fig. S3) exhibited three fitted peaks at 399.2 eV, 399.8 eV, and 401.2 eV corresponding to N-$(C)_3$, C-N, and N–H, respectively. The high-resolved O1s spectrum (Fig. S4) was well-fitted into two peaks located at 531 eV and 532.6 eV,

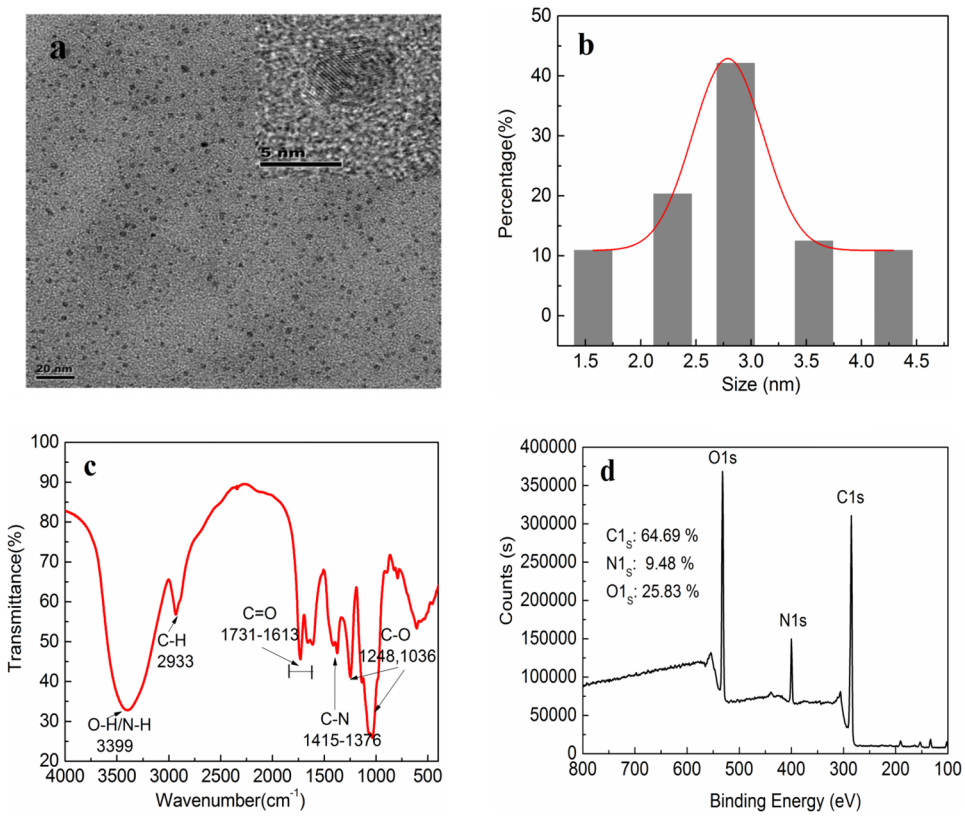

Fig. 1 **a** A typical HR-TEM image of N-CDs. **b** Diameter size distribution. **c** FT-IR spectrum of N-CDs. **d** The XPS survey spectrum

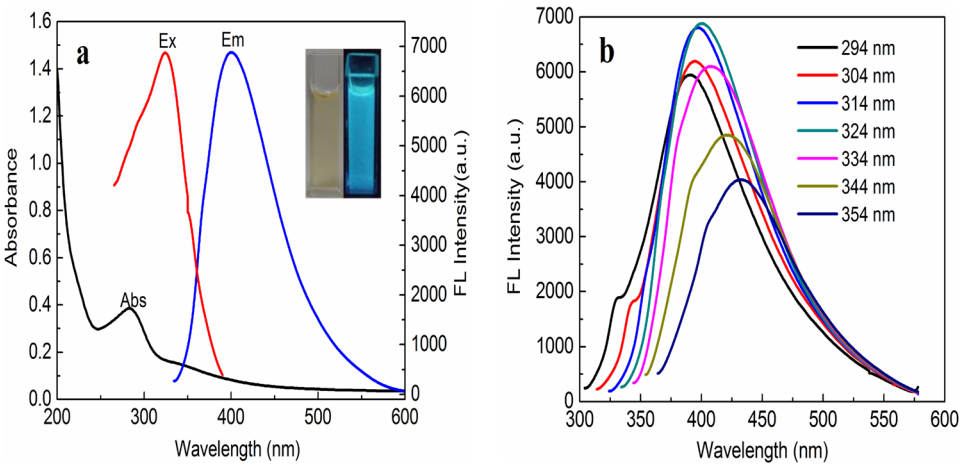

Fig. 2 **a** UV–vis absorbance (black line), fluorescence excitation (red line), and emission (blue line) spectra of N-CDs (inset: photographs of N-CDs in aqueous solution under visible light (left) and 365-nm UV lamp (right)). **b** FL spectra of N-CDs at different λex (294 nm–354 nm)

thus demonstrating the presence of C = O and C-O on the surface of N-CDs. Results of XPS were well consistent with the FT-IR. The FT-IR and XPS data demonstrate that the surface of the N-CDs is rich in carboxyl, amino, hydroxyl, and other hydrophilic groups [48–54].

3.2 Optical properties of the N-CDs

The optical properties of the N-CDs were explored by UV–vis absorption and fluorescence spectra at room temperature. An obvious absorption peak centered at 284 nm in the UV–vis absorption spectrum (Fig. 2a) could be ascribed to the π-π* transition of C = C bond [55]. The N-CD solution was pale brown and transparent under sunlight and exhibited bright blue light under a 365-nm UV lamp, as shown in Fig. 2a (inset). When the excitation wavelength of N-CDs is at 324 nm, the maximum fluorescence emission peak is centered at 400 nm. The fluorescence spectra of N-CDs were recorded with the increase of the excitation wavelength from 294 to 354 nm in 10-nm increments. The N-CDs have an excitation-dependent emission behavior similar to most of the CDs reported in the literature (Fig. 2b) [48]. The N-CDs exhibited great anti-photobleaching property and photostability under high concentration NaCl solution. The fluorescence intensities of N-CDs changed slightly under 40 min UV irradiation (Fig. S5) and 1 mol·L^{-1} NaCl solution (Fig. S6). And the fluorescence properties of the N-CD solution stored at 4 °C were almost unchanged for 2 months. Excellent stability of N-CDs facilitates the fluorescence probe in complex matrixes.

3.3 Fluorescence quenching mechanism of MnO_4^-

Figure 3a shows considerable overlap between the excitation or emission spectrum of N-CDs and the UV absorption band of MnO_4^-. The inner filter effect (IFE) may be formed between N-CDs and MnO_4^- leading to fluorescence quenching of N-CDs. The fluorescence lifetimes of N-CDs and N-CDs with 3 μM MnO_4^- were recorded to further explore the fluorescence quenching mechanism of MnO_4^-. As shown in Fig. S7, the fluorescence lifetime was almost unchanged after the addition of MnO_4^-, which suggested

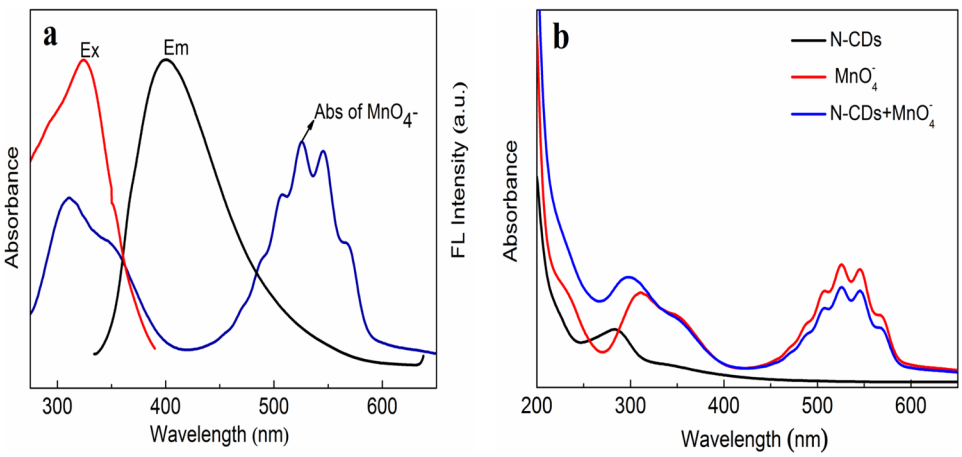

Fig. 3 **a** The UV–vis absorbance of MnO_4^- (blue line), the fluorescence excitation (red line), and emission (black line) spectra of N-CDs. **b** The UV–vis absorbance of N-CDs, MnO_4^-, and N-CDs after the addition of MnO_4^-

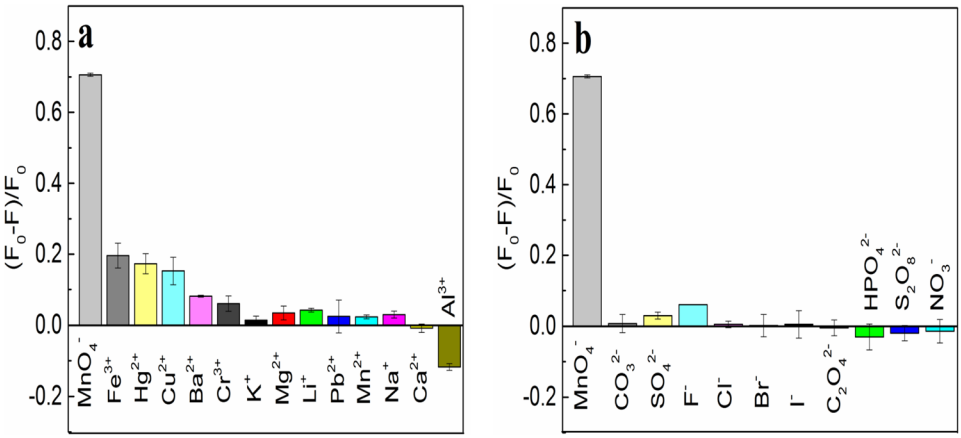

Fig. 4 Effects of metal cations (**a**) and anion (**b**) on the FL probe of MnO_4^-. Concentrations of the interference and MnO_4^- were all 50 μM

that the fluorescence quenching of N-CDs was not caused by dynamic quenching or fluorescence resonance energy transfer [55, 56]. In addition, the UV absorption spectra of N-CDs obviously changed (Fig. 3b): The intensity of the UV absorption peak (284 nm) of N-CDs increased with an obvious redshift. There were broad absorption peaks in the range of 450–600 nm in the UV absorbance spectrum of N-CDs with MnO_4^-, which indicated the static complex or chelate was formed between MnO_4^- and N-CDs [49]. In conclusion, the fluorescence quenching of N-CDs was due to static quenching and IFE.

3.4 Analytical performance of MnO_4^- detection

3.4.1 Selectivity of the fluorescent probe

To explore the anti-interference performance of the fluorescent probe to the sensing of MnO_4^-, under the same experimental conditions, the effects of some metal cations (Fe^{3+}, Hg^{2+}, Cu^{2+}, Ba^{2+}, Cr^{3+}, K^+, Mg^{2+}, Li^+, Pb^{2+}, Mn^{2+}, Na^+, and Ca^{2+}) and anions (CO_3^{2-}, SO_4^{2-}, F^-, Cl^-, Br^-, I^-, $C_2O_4^{2-}$, HPO_4^{2-}, $S_2O_8^{2-}$, and NO_3^-) on the fluorescence intensity of N-CDs were investigated by adding the same concentrations (50 μM) of MnO_4^- and potential interference substances. Figure 4a and b show that the largest $(F_0-F)/F_0$ was obtained upon addition of MnO_4^- where F_0 and F were the fluorescence intensities of N-CDs without and with metal cations or anions, respectively. The fluorescence intensity of N-CDs decreased sharply upon addition of MnO_4^-, but all other metal cations and anions had a negligible effect on the fluorescence intensity of N-CDs. These results suggested that the fluorescence probe based on N-CDs had excellent selectivity and strong tolerance to the detection of MnO_4^-.

3.4.2 Optimization of detection conditions

The influence of pH and reaction time were optimized to obtain a high sensitivity (Fig. 5a and b). The fluorescence intensity with or without MnO_4^- was pH-dependent from 2 to 13. The highest quenching effect was obtained at pH 2. Furthermore, the fluorescence intensity of the N-CDs decreased immediately upon addition of 1.5 μM MnO_4^-, and the F/F_0 remained constant when the incubation time was 20 min. F_0 and F were the fluorescence intensities of N-CDs

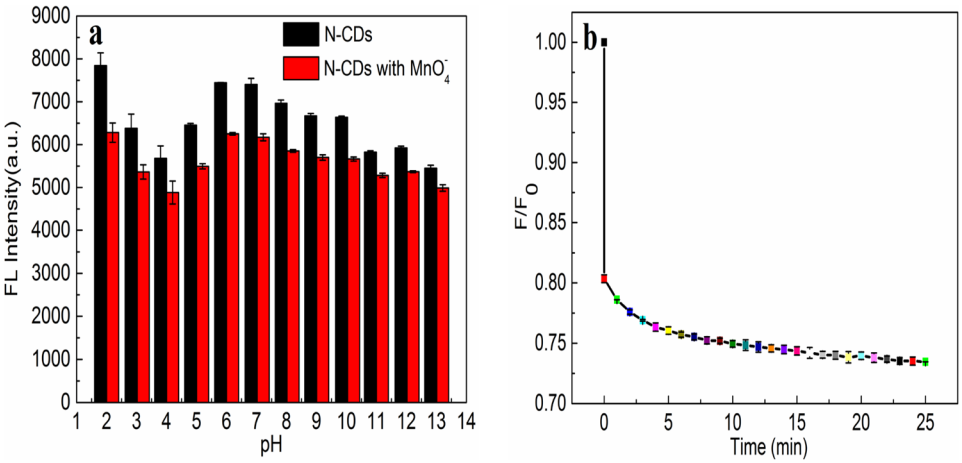

Fig. 5 **a** Effect of pH on the fluorescence intensity of N-CDs before and after the addition of MnO_4^- (1.5 μM). **b** Effect of reaction time on the fluorescence intensity of N-CDs and MnO_4^- system

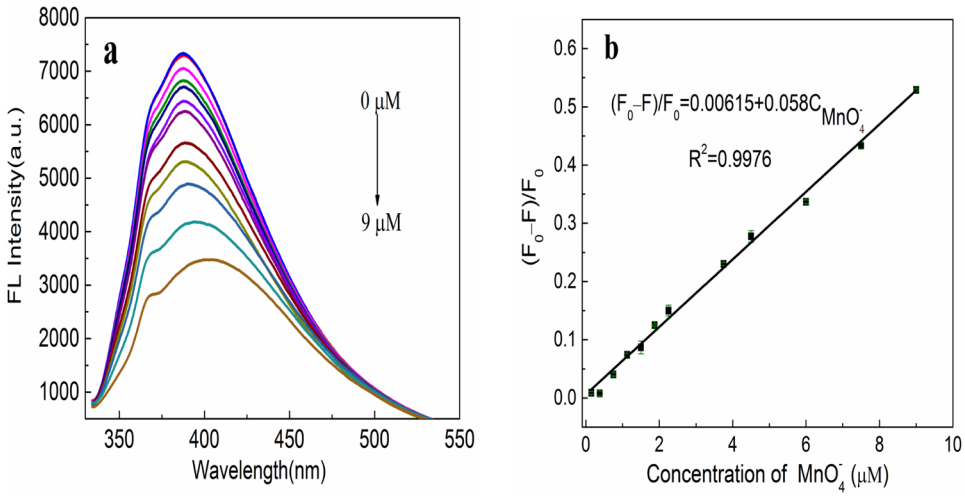

Fig. 6 **a** Fluorescence spectra of N-CDs with different concentrations of MnO_4^-. **b** Relationship between the ratio of $(F_0-F)/F_0$ and the concentration of MnO_4^- from 0.15 to 9.00 μM

without and with 1.5 μM MnO_4^-, respectively. Hence, pH 2 and 20 min were used as the optimal pH and reaction time in the later work.

3.4.3 Fluorescenceresponse to MnO_4^-

Figure 6a shows that the fluorescence intensity of N-CDs decreased gradually with increasing MnO_4^- concentration. The fluorescence quenching effect of the system is linear with the concentration of MnO_4^- from 0.15 to 9.00 μM (Fig. 6b). A linear equation was thus established as $(F_0-F)/F_0=0.00615+0.058\ C_{MnO_4^-}$ (μM), $R^2=0.9976$, where F_0 and F were the fluorescence intensities of N-CDs without and with different concentrations of MnO_4^-, respectively. The limit of detection (LOD) of MnO_4^- was determined to be 0.12 μM according to the equation LOD = $3\sigma/k$, where σ is standard deviation of the blank solution ($n=11$) and k is the slope of the regression line [47].

The results of the proposed fluorescent probe were also compared to the reported literature, as shown in Table 1.

Table 1 Comparison of the reported methods for the analysis of MnO_4^-

Detection method	Linear range (μM)	LOD (μM)	References
Uranyl organic framework	0–475	1.79	[6]
Mn-doped CDs	3–150	0.66	[57]
CDs@MOF(Eu)	0–32	0.68	[3]
COF	0–1000	10	[58]
AuNCs@PAMAM	0–10	0.56	[12]
N-CDs	0.15–9.00	0.12	This work

This novel probe offers high sensitivity and low detection limits for MnO_4^-, suggesting that it has great potential for the detection of MnO_4^- in simulation samples.

3.4.4 Simulation sample analysis

The proposed fluorescent probe was successfully used for the detection of MnO_4^- in polluted water to confirm that the method is accurate and reliable. The simulation sample analysis was carried out as follows. For FL spectra, 200 μL of pure N-CD solution, 200 μL polluted water, and different amounts of MnO_4^- solution were successively transferred into a 1-cm quartz cuvette, and the mixture was diluted with PBS buffer solution (pH = 2) to a final volume of 2 mL, and this was then mixed thoroughly. The mixed solution was then incubated for 20 min at room temperature. The results are shown in Table 2. The recoveries were 99.4–101.2%, and the relative standard deviations (RSD) were in the range of 2.12 to 3.93%. Thus, the results suggest that the N-CDs can offer trace MnO_4^- detection in simulation samples.

Table 2 Analysis of MnO_4^- in polluted water

Sample	Spiked (μM)	Found (μM)	Recovery (%, $n=3$)	RSD (%, $n=3$)
Polluted water	0	ND	–	–
	1.125	1.117	99.4	2.29
	1.875	1.889	101.2	3.93
	3.000	2.999	100.5	2.12

ND not detected

4 Conclusions

Auricularia auricula (L.ex Hook.) Underw was used to synthesize N-CDs via a facile hydrothermal method in this study. The FL intensity of the synthesized N-CDs could be selectively and sensitively quenched by MnO_4^-. There was a good linear relationship between the FL response and the concentration of MnO_4^- from 0.15 to 9.00 μM with the detection limit of 0.12 μM. The fluorescence quenching of N-CDs was caused by static quenching and IFE. A fluorescent probe was developed and successfully used to quantitatively detect MnO_4^- in polluted water with good recoveries from 99.4 to 101.2%. The fluorescent probe is highly sensitive, selective, low cost, environmentally friendly, and easy to prepare. Thus, it has great potential for quantitative monitoring of MnO_4^- in simulation samples.

Supplementary Information The online version contains supplementary material available at https://doi.org/10.1007/s42114-022-00443-0.

Funding Financial support from the National Natural Science Foundation of China (No. 21465024 and No. 21765023), the Local Undergraduate Colleges and Universities in Yunnan province (part) joint specific fund project (No. 2019FH001(-112)), Research Foundation of the Education Department of Yunnan Province (No. 2019J0737), the Program for Innovation Research Team in Science and Technology in University of Yunnan Province, and the Provincial Undergraduate Innovation and Entrepreneurship Program (Nos. 202111390039 and 2021A010) are gratefully acknowledged. We thank LetPub (www.letpub.com) for linguistic assistance and pre-submission expert review.

Declarations

Conflict of interest The authors declare no competing interests.

References

1. Jiang XH, Qin DM, Mo GC, Feng JS, Zheng XF, Deng BY (2019) Facile preparation of boron and nitrogen codoped green emission carbon quantum dots for detection of permanganate and captopril. Anal Chem 91(17):11455–11460
2. Ye Z, Weng R, Ma Y, Wang F, Liu H, Wei L, Xiao L (2018) Label-free single-particle colorimetric detection of permanganate by GNPs@Ag core-shell nanoparticle with dark-field optical microscopy. Anal Chem 90(21):13044–13050
3. Fu X, Lv R, Su J, Li H, Liu X (2018) A dual-emission nano-rod MOF equipped with carbon dots for visual detection of doxycycline and sensitive sensing of MnO_4^-. RSC Adv 8(9):4766–4772
4. Liu F, Li H, Liao D, Xu Y, Yu M, Deng S, Zhang G, Xiao T, Long J, Zhang H, Li Y, Li K, Zhang P (2020) Carbon quantum dots derived from the extracellular polymeric substance of anaerobic ammonium oxidation granular sludge for detection of trace Mn(VII) and Cr(VI). RSC Adv 10(53):32249–32258
5. Ding B, Liu SX, Cheng Y, Guo C, Wu XX, Guo JH, Liu YY, Li Y (2016) Heterometallic alkaline earth - lanthanide BaII - LaIII microporous metal-organic framework as bifunctional luminescent probes of Al^{3+} and MnO_4^-. Inorg Chem 55(9):4391–4402
6. Wang L, Tu B, Xu W, Fu Y, Zheng Y (2020) Uranyl organic framework as a highly selective and sensitive turn - on and turn - off luminescent sensor for dual functional detection arginine and MnO_4^-. Inorg Chem 59(7):5004–5017
7. Citak D, Tuzen M, Soylak M (2010) Speciation of Mn(II), Mn(VII) and total manganese in water and food samples by coprecipitation–atomic absorption spectrometry combination. J Hazard Mater 173(1):773–777
8. Chen S, Qin X, Gu W, Zhu X (2016) Speciation analysis of Mn(II)/Mn(VII) using Fe_3O_4@ionic liquids-β-cyclodextrin polymer magnetic solid phase extraction coupled with ICP-OES. Talanta 161:325–332
9. Grygo-Szymanko E, Tobiasz A, Miliszkiewicz N, Dudek-Adamska D, Walas S (2017) Evaluation of manganese(II) and manganese(VII) speciation in water samples by ion pair high-performance liquid chromatography-inductively coupled plasma mass spectrometry. Anal Lett 50(13):2147–2160
10. Chen S, Zhan X, Lu D, Yang M (2008) Study on adsorption behavior of Mn(II) and Mn(VII) on modified carbon nanofibers and their determination by inductively coupled plasma mass spectrometry. Atom Spectrosc 29:45–50
11. Qiu B, Xue L, Wu Y, Lin Z, Guo L, Chen G (2011) Mechanism study on inorganic oxidants induced inhibition of $Ru(bpy)_3^{2+}$ electrochemiluminescence and its application for sensitive determination of some inorganic oxidants. Talanta 85(1):339–344
12. Yang L, Wang H, Li D, Li L, Lou X, Liu H (2018) Self-nucleation and self-assembly of highly fluorescent Au 5 nanoclusters for bioimaging. Chem Mater 30(15):5507–5515
13. Xu S, Shi JJ, Ding B, Liu ZY, Wang XG, Zhao XJ, Yang EC (2019) A heterometallic sodium(i)-europium(iii)-organic layer exhibiting dual-responsive luminescent sensing for nitrofuran antibiotics, $Cr_2O_7^{2-}$ and MnO_4^- anions. Dalton T 48(5):1823–1834
14. Sun Z, Sun J, Xi L, Xie J, Wang X, Ma Y, Li L (2020) Two novel lanthanide metal-organic frameworks: selective luminescent sensing for nitrobenzene, Cu^{2+}, and MnO_4^-. Cryst Growth Des 20(8):5225–5234
15. Zhu K, Fan R, Zheng X, Wang P, Chen W, Sun T, Gai S, Zhou X, Yang Y (2019) Dual-emitting dye-CDs@MOFs for selective and sensitive identification of antibiotics and MnO_4^- in water. J Mater Chem C 7(47):15057–15065
16. Wu Y, Liu D, Lin M, Qian J (2020) Zinc(ii)-based coordination polymer encapsulated Tb^{3+} as a multi-responsive luminescent sensor for Ru^{3+}, Fe^{3+}, CrO_4^{2-}, $Cr_2O_7^{2-}$ and MnO_4^-. RSC Adv 10(10):6022–6029
17. Wang YN, Wang SD, Gao YM, Yang LL, Xie LX (2019) 3D cadmium(II)-based coordination polymer constructed from v-shaped semirigid ligand: selective detection of oxoanion pollutants CrO_4^{2-}, $Cr_2O_7^{2-}$, MnO_4^- in water. Z Anorg Allg Chem 645(24):1358–1364
18. Su W, Wu H, Xu H, Zhang Y, Li Y, Li X, Fan L (2020) Carbon dots: a booming material for biomedical applications. Mater Chem Front 4(3):821–836
19. Shuang E, Mao QX, Wang JH, Chen XW (2020) Carbon dots with tunable dual emissions: from the mechanism to the specific imaging of endoplasmic reticulum polarity. Nanoscale 12(12):6852–6860
20. Guo J, Li X, Liu H, Young DP, Song G, Song KN, Zhu JF, Kong J, Guo ZH (2021) Tunable magnetoresistance of core-shell structured polyaniline nanocomposites with 0-, 1-, and 2-dimensional nanocarbons. Adv Compos Hybrid Mater 4(1):51–64
21. Hettiarachchi SD, Graham RM, Mintz KJ, Zhou Y, Vanni S, Peng Z, Leblanc RM (2019) Triple conjugated carbon dots as a nano-drug delivery model for glioblastoma brain tumors. Nanoscale 11(13):6192–6205
22. Xu D, Lin Q, Chang HT (2019) Recent advances and sensing applications of carbon dots. Small Methods 4:1900387
23. Ma XY, Zhong W, Zhao J, Suib SL, Lei Y (2020) "Self-heating" enabled one-pot synthesis of fluorescent carbon dots. Eng Sci 9:44–49

24. Kumari M, Chaudhary GR, Chaudhary S, Umar A (2022) Rapid analysis of trace sulphite ion using fluorescent carbon dots produced from single use plastic cups. Eng Sci 17:101–112
25. Li H, Yan X, Kong D, Jin R, Sun C, Du D, Lin Y, Lu G (2020) Recent advances in carbon dots for bioimaging applications. Nanoscale Horiz 5(2):218–234
26. Zhang Z, Yi G, Li P, Zhang X, Fan H, Zhang Y, Wang X, Zhang C (2020) A minireview on doped carbon dots for photocatalytic and electrocatalytic applications. Nanoscale 12(26):13899–13906
27. Wu H, Zhong YM, Tang YX, Huang YQ, Liu G, Sun WT, Xie PT, Pan D, Liu CZ, Guo ZH (2021) Precise regulation of weakly negative permittivity in $CaCu_3Ti_4O_{12}$ metacomposites by synergistic effects of carbon nanotubes and grapheme. Adv Compos Hybrid Mater. https://doi.org/10.1007/s42114-021-00378-y
28. Qi GY, Liu Y, Chen LL, Xie PT, Pan D, Shi ZC, Quan B, Zhong YM, Liu CZ, Fan RH, Guo ZH (2021) Lightweight Fe_3C@Fe/C nanocomposites derived from wasted cornstalks with high-efficiency microwave absorption and ultrathin thickness. Adv Compos Hybrid Mater 4(4):1226–1238
29. Xie PT, Liu Y, Feng M, Niu M, Liu CZ, Wu NN, Sui KY, Patil RR, Pan D, Guo ZH, Fan RH (2021) Hierarchically porous Co/C nanocomposites for ultralight high-performance microwave absorption. Adv Compos Hybrid Mater 4(1):173–185
30. Wu HK, Sun HW, Han FJ, Xie PT, Zhong YM, Quan B, Zhao YM, Liu CZ, Fan RH, Guo ZH (2022) Negative permittivity behavior in flexible carbon nanofibers-polydimethylsiloxane films. Eng Sci 17:113–120
31. Wang W, Deng XJ, Liu DQ, Luo F, Cheng HF, Cao TS, Li YL, Deng YJ, Xie W (2021) Broadband radar-absorbing performance of square-hole structure. Adv Compos Hybrid Mater. https://doi.org/10.1007/s42114-021-00376-0
32. Guo J, Li X, Chen ZR, Zhu JF, Mai XM, Wei RB, Sun K, Liu H, Chen YX, Naik N, Guo ZH (2022) Magnetic $NiFe_2O_4$/polypyrrole nanocomposites with enhanced electromagnetic wave absorption. J Mater Sci Technol 108:64–72
33. Yan F, Zhang H, Yu N, Sun Z, Chen L (2021) Conjugate area-controlled synthesis of multiple-color carbon dots and application in sensors and optoelectronic devices. Sensor Actuat B Chem 329:129263
34. Sun Z, Qu KQ, Li JH, Yang S, Yuan BN, Huang ZH, Guo ZH (2021) Self-template biomass-derived nitrogen and oxygen co-doped porous carbon for symmetrical supercapacitor and dye adsorption. Adv Compos Hybrid Mater 4(4):1413–1424
35. Jiang X, Chen Y, Meng X, Cao W, Liu C, Huang Q, Naik N, Murugadoss V, Huang M, Guo Z (2022) The impact of electrode with carbon materials on safety performance of lithium-ion batteries: a review. Carbon 191:448–470
36. Tan L, Wei C, Zhang Y, An Y, Xiong S, Feng J (2022) Long-life and dendrite-free zinc metal anode enabled by a flexible, green and self-assembled zincophilic biomass engineered MXene based interface. Chem Eng J 431:134277
37. Wareing TC, Gentile P, Phan AN (2021) Biomass-based carbon dots: current development and future perspectives. ACS Nano 15(10):15471–15501
38. Kang C, Huang Y, Yang H, Yan XF, Chen ZP (2020) A review of carbon dots produced from biomass wastes. Nanomaterials 10:2316
39. Zhu EQ, Xu GF, Sun SF, Yang J, Yang HY, Wang DW, Guo ZH, Shi ZJ, Deng J (2021) Rosin acid modification of bamboo powder and thermoplasticity of its products based on hydrothermal pretreatment. Adv Compos Hybrid Mater 4(3):584–590
40. Deng ZH, Deng Q, Wang LQ, Xiang P, Lin J, Murugadoss V, Song G (2021) Modifying coconut shell activated carbon for improved purification of benzene from volatile organic waste gas. Adv Compos Hybrid Mater 4(3):751–760
41. Wang Y, Hu YJ, Hao X, Peng P, Shi JY, Peng F, Sun RC (2020) Hydrothermal synthesis and applications of advanced carbonaceous materials from biomass: a review. Adv Compos Hybrid Mater 3(3):267–284
42. Zulfajri M, Rasool A, Huang G (2020) A fluorescent sensor based on oyster mushroom-carbon dots for sensing nitroarenes in aqueous solutions. New J Chem 44:10525–10535
43. Zhu Z, Yang P, Li X, Luo M, Zhang W, Chen M, Zhou X (2019) Green preparation of palm powder-derived carbon dots co-doped with sulfur/chlorine and their application in visible-light photocatalysis. Spectrochim Acta A 227:117659
44. Wu L, Long R, Li T, Tang C, Tong X, Guo Y, Shi S, Xiang H, Tong C (2020) One-pot fabrication of dual-emission and single-emission biomass carbon dots for Cu^{2+} and tetracycline sensing and multicolor cellular imaging. Anal Bioanal Chem 412(27):7481–7489
45. Wongso V, Sambudi NS, Sufian S, Isnaeni (2021) The effect of hydrothermal conditions on photoluminescence properties of rice husk-derived silica-carbon quantum dots for methylene blue degradation. Biomass Convers Biorefin 11(6):2641–2654
46. Vijeata A, Chaudhary GR, Umar A, Chaudhary S (2021) Distinctive solvatochromic response of fluorescent carbon dots derived from different components of Aegle Marmelos plant. Eng Sci 15:197–209
47. Khan ZMSH, Saifi S, Shumaila Aslam Z, Khan SA, Zulfequar M (2020) A facile one step hydrothermal synthesis of carbon quantum dots for label-free fluorescence sensing approach to detect picric acid in aqueous solution. J Photoch Photobio A 388:112201
48. Zhang Z, Hu B, Zhuang Q, Wang Y, Luo X, Xie Y, Zhou D (2020) Green synthesis of fluorescent nitrogen–sulfur co-doped carbon dots from scallion leaves for hemin Sensing. Anal Lett 53(11):1704–1718
49. Hu G, Ge L, Li Y, Mukhtar M, Shen B, Yang D, Li J (2020) Carbon dots derived from flax straw for highly sensitive and selective detections of cobalt, chromium, and ascorbic acid. J Colloid Interface Sci 579:96–108
50. Guo J, Chen ZR, Abdul W, Kong J, Khan MA, Young DP, Zhu JF, Guo ZH (2021) Tunable positive magnetoresistance of magnetic polyaniline nanocomposites. Adv Compos Hybrid Mater 4(3):534–542
51. Pan D, Dong JW, Yang G, Su FM, Chang BB, Liu CT, Zhu YC, Guo ZH (2021) Ice template method assists in obtaining carbonized cellulose/boron nitride aerogel with 3D spatial network structure to enhance the thermal conductivity and flame retardancy of epoxy-based composites. Adv Compos Hybrid Mater. https://doi.org/10.1007/s42114-021-00362-6
52. Qu KQ, Sun Z, Shi C, Wang WC, Xiao LD, Tian JY, Huang ZH, Guo ZH (2021) Dual-acting cellulose nanocomposites filled with carbon nanotubes and zeolitic imidazolate framework-67 (ZIF-67)–derived polyhedral porous Co_3O_4 for symmetric supercapacitors. Adv Compos Hybrid Mater 4(3):670–683
53. Liu S, Du HS, Liu K, Ma MG, Kwon YE, Si CL, Ji XX, Choi SE, Zhang XY (2021) Flexible and porous Co_3O_4-carbon nanofibers as binder-free electrodes for supercapacitors. Adv Compos Hybrid Mater 4(4):1367–1383
54. Algadi H, Albargi H, Umar A, Shkir M (2021) Enhanced photoresponsivity of anatase titanium dioxide (TiO_2)/nitrogen-doped graphene quantum dots (N-GQDs) heterojunction-based photodetector. Adv Compos Hybrid Mater 4(4):1354–1366
55. Long C, Qing T, Fu Q, Jiang Z, Xu J, Zhang P, Feng B (2020) Low-temperature rapid synthesis of high-stable carbon dots and its application in biochemical sensing. Dyes Pigments 175:108184
56. Tong X, Li T, Long R, Guo Y, Wu L, Shi S (2020) Determination of the activity of γ-glutamyl transpeptidase and of its inhibitors by using the inner filter effect on the fluorescence of nitrogen-doped carbon dots. Microchim Acta 187(3):182
57. Chu X, Ning G, Zhou Z, Liu Y, Xiao Q, Huang S (2020) Bright Mn-doped carbon dots for the determination of permanganate and L-ascorbic acid by a fluorescence on-off-on strategy. Microchim Acta 187(12):659

58. Huang M, Chong J, Hu C, Yang Y (2020) Ratiometric fluorescent detection of temperature and MnO_4^- using a modified covalent organic framework. Inorg Chem Commun 119:108094